PHOTONICS Research

Plasmon-enhanced fluorescence of gold nanoparticle/graphene quantum dots for detection of Cr^{3+} ions

You-Long Chen,[1,2,3] Yi-Hua Hu,[1,2,3,4] Xing Yang,[1,2,3] You-Lin Gu,[1,2,3] Xin-Yu Wang,[1,2,3] Yu-Hao Xia,[1,2,3] Xin-Yuan Zhang,[1,2,3] and Yu-Shuang Zhang[1,2,3,5]

[1]State Key Laboratory of Pulsed Power Laser Technology, National University of Defense Technology, Hefei 230037, China
[2]Key Laboratory of Electronic Restriction of Anhui Province, National University of Defense Technology, Hefei 230037, China
[3]Advanced Laser Technology Laboratory of Anhui Province, Hefei 230037, China
[4]e-mail: skl_hyh@163.com
[5]e-mail: yszhang@hnu.edu.cn

Received 18 May 2023; revised 17 July 2023; accepted 25 July 2023; posted 28 July 2023 (Doc. ID 495683); published 1 October 2023

Graphene quantum dots (GQDs), fascinating semiconductors with stable photoluminescence (PL), have important potential applications in the fields of biology, medicine, and new semiconductor devices. However, it is still challenging to overcome the weak PL intensity. Here, we report a strategy for selective resonance enhancement of GQD fluorescence using gold nanoparticles (AuNPs) as plasmas. Interestingly, the addition of low concentration AuNP makes AuNP/GQDs exhibit significant fluorescence enhancement of 2.67 times in the visible range. The addition of high concentration AuNP leads to the formation of an excitation peak at 421 nm and selectively enhances certain radiation modes. We concluded that the main reason for the selective enhancement of PL intensity in high concentration AuNP is the transfer of generous hot electrons at high energy states from AuNP to GQD and relaxation to the ground state. The electron resonance of low concentration AuNP transfers to GQD and relaxes to lower energy levels, exhibiting an overall enhancement of PL intensity. We apply it for detection of the heavy metal ion Cr^{3+}, and verify that it has a correlation coefficient of 97.36%. We believe AuNP/GQDs can be considered excellent candidates for heavy metal detection and high fluorescence bio-imaging.

https://doi.org/10.1364/PRJ.495683

1. INTRODUCTION

With the occurrence of heavy metals in blood, drinking water, and growing environmental pollution, great attention has been paid to heavy metal ion detection with high sensitivity and selectivity [1]. Cr^{3+} is considered harmful to humans due to its strong oxidation properties and easy penetration of biological membranes [2,3]. Electrochemical methods, atomic absorption spectrometry, and coupled plasma mass spectrometry have been developed [4–6] to measure the concentration of Cr^{3+}. Nevertheless, the use of bulky instruments is costly, inconvenient, and unfeasible for on-site measurement of pollutants. Therefore, a simple, low cost, highly sensitive detection method that can detect chromium concentration in drinking water and the human body is highly desired.

As 0D material, graphene quantum dots (GQDs) have aroused great interest in research and practical applications due to their superior and exciting chemical, physical, mechanical, and electronic properties [7]. They have open bandwidths due to quantum confinement, excellent dispersibility, and more abundant active sites [8–10]. GQDs have the excellent performance required for biomedical applications such as biocompatibility, which gives them unique advantages in heavy metal sensing. The enhanced photoluminescence (PL) emission of GQDs can improve their performance in photoelectric detectors and minimize the effect of different noises on the efficiency of such devices, resulting in higher sensitivity [11,12].

The PL intensity of a fluorescent molecule can be strongly enhanced when near a metal nanoparticle (NP) [13,14]. Localized surface plasmon (LSP) resonance enhanced PL has gained considerable attention in numerous applications and research areas, such as biology and medical science [15–18]. It is necessary to understand the mechanism for such a good effect if we intend to develop better materials to improve the enhancement. Usually, PL enhancement can be attributed to two means: a localized enhanced electric field [19] and plasmon resonance energy transfer [20]. A localized enhanced electric field refers to the local electric field generated by photoexcited plasmon crystals, and the PL emission of fluorescent molecules increases under a strong local electric field [21,22]. Plasmon resonance energy transfer is similar mechanism [23,24].

The process can be described as follows: the plasmon crystals absorb photons and excite plasmon resonance, and energy is transferred to fluorescent molecules through intraband excitations within the conduction band or through interband excitations caused by transitions between other bands (for example, D bands) and the conduction band. The donor transfers rich hot carriers on the surface of the acceptor molecule through the dipole–dipole coupling of non-radiation. However, the mechanism of PL enhancement is too complex to distinguish which mechanism plays a major role [25].

In our work, GQDs were attached to the surface of a gold NP (AuNP) to enhance PL intensity selectively. To investigate whether the localized enhanced electric field or plasmon resonance energy transfer is the main mechanism of PL enhancement, we conducted a control experiment to isolate the adiabatic electron transfer path and adjust the AuNP near field strength. It proved that AuNP plays the role of a dipolar antenna, mainly by collecting incoming photons from a range much larger than GQDs' and transferring hot electrons to the electron transition path of electron–hole recombination in the GQDs' electronic structure. Density functional theory (DFT), Raman spectrum, time-resolved PL (TRPL) decays, and the PL spectrum proved that the reason for selective fluorescence enhancement or overall enhancement of graphene is that due to the addition of different concentrations of AuNP, the electrons directly relax from the high energy band to the ground state or a lower energy level and then return to the ground state.

2. RESULTS AND DISCUSSION

AuNPs were prepared by a modified seed-mediated method. To verify the crystal nature of the AuNP/GQDs, Figs. 1(a) and 1(b) show the representative transmission electron microscopy (TEM) and high angle annular dark-field-scanning TEM (HADDF-STEM) images of AuNP/GQDs. The diameter of AuNP coated randomly with GQDs was 21.6 ± 2.4 nm [Figs. 2(a)–2(c)]. The high resolution TEM (HRTEM) image [Fig. 1(c)] clearly indicates that GQDs were attached on the surface of AuNP. The marked distance of the straight fringes in GQDs is around 0.21 nm, which corresponds to the (100) plane of GQDs. The corresponding selected area electron diffraction (SAED) pattern in Fig. 1(d) demonstrates the good crystallinity of AuNP. The concentric rings can be assigned to the (111), (200), (220), and (311) planes of Au.

X-ray photoelectron spectroscopy (XPS) confirmed the presence of electron donors and electron acceptors. Figure 3 shows XPS spectra containing GQD and AuNP/GQDs in which AuNP/GQDs = 400:4. Deconvolution of the C 1s spectrum [Fig. 3(a)] resulted in the observation of C═C, C═O, and ─COOH bonds with binding energies of 284.6 eV, 286.7 eV, and 288.4 eV, respectively [26,27]. Deconvolution of the O 1s spectrum [Fig. 3(b)] resulted in the observation of C═O and C─O bonds with binding energies of 531.6 eV and 533.2 eV, respectively [26,27]. The ratio of the different groups in GQDs and AuNP/GQDs is shown in Fig. 3(c). XPS results indicate that a relative proportion of the electron donor group (─OH) and electron acceptor carboxy ─COOH in AuNP/GQDs has no significant changes relative to GQDs. In addition, the peak in Fig. 3(d) is attributed to the 4f electron of

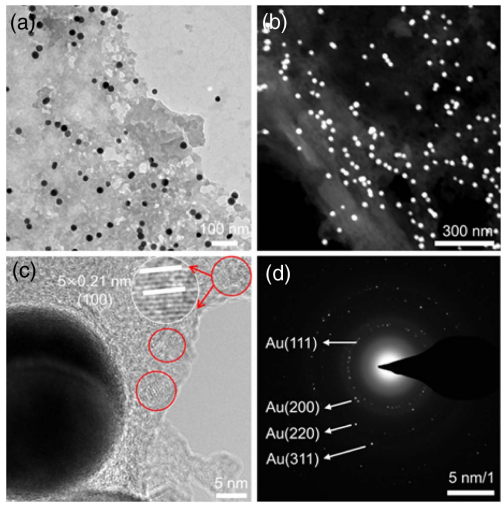

Fig. 1. (a) Representative transmission electron microscopy (TEM) and (b) high angle annular dark-field-scanning transmission electron microscopy (HADDF-STEM) images of the AuNP/GQDs. (c) High resolution transmission electron microscopy (HRTEM) image of the AuNP/GQDs; the red circle inside is GQD, inset is a scaled up view of GQD with high resolution, lattice spacing is 0.21 nm, and crystal plane is (100). (d) Selected area electron diffraction (SAED) pattern of AuNP/GQDs.

Au, which further indicates the existence of AuNPs. The Raman spectrum [Fig. 3(e)] of AuNP/GQDs and GQDs shows three prominent peaks at 1345 cm^{-1}, 1585 cm^{-1}, and 2685 cm^{-1}, corresponding to the disordered sp^3 hybrid defect structure (D), ordered sp^2 graphite carbon structure (G), and second order of the D (2D) band [28], respectively. There is a slight blueshift in the peak positions of AuNP/GQDs compared to individual GQDs [29]. The blueshift is attributed to the coupling between GQDs and AuNP plasmons [30]. A decreased intensity ratio (I_G/I_D) for AuNP/GQDs (from 0.80 to 0.76) indicates that plasmon resonance can reduce the local distortion of sp^2-hybrid carbons [31], the charge transfer from AuNP [32] to GQDs, and the enhanced electron–phonon coupling [30,33]. The Fourier transform infrared (FTIR) spectra shown in Fig. 3(f) reveal that there is no noticeable change in the surface GQDs and AuNP/GQDs, both of which possess abundant hydrophilic groups such as COOH (1759 cm^{-1}), ─C═O (1743 cm^{-1}), and C─O (1258 cm^{-1}) on their surfaces. Moreover, stretching vibrations of C─N═(1427 cm^{-1}) bonds were observed, indicating the polyaromatic structures in GQDs and AuNP/GQDs.

We systematically studied the spectral properties of the materials. Figure 4(a) shows the ultraviolet-visible (UV-Vis) absorption spectra of AuNP/GQDs and GQDs. A typical absorption peak at 300 nm along with an extension that proceeds to the visible region was observed, which was inferred to the π–π^* transition of C═C and n–π^* transition of C═O in the nanocarbon [34]. The broad absorption spectra indicate that the GQDs have multiple electron transition paths instead of a well-defined bandgap. The stronger absorption capacity demonstrates that AuNP/GQDs have a stronger ability to trap photons. The absorption peak at 527 nm is attributed to

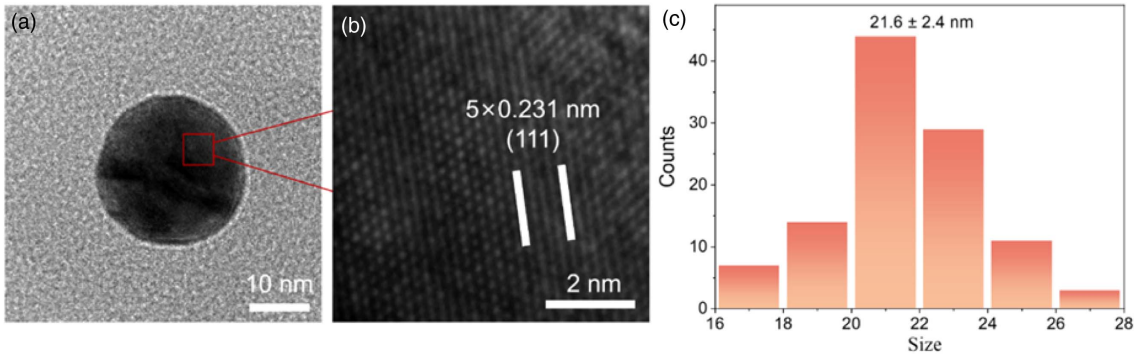

Fig. 2. (a) Representative transmission electron microscopy (TEM) and (b) high resolution transmission electron microscopy (HRTEM) images in the red region of AuNPs. (c) Statistical diameter of AuNPs.

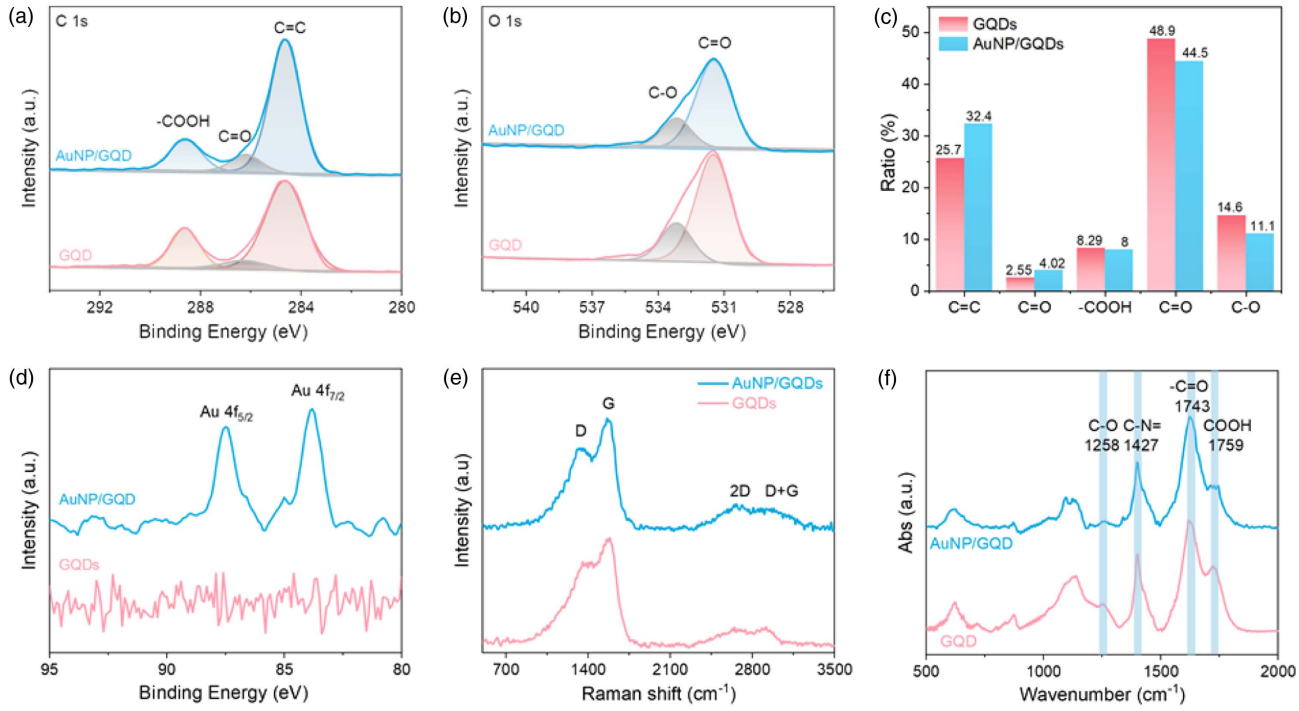

Fig. 3. (a) Binding energies correspond to the C 1s of GQDs and (b) O 1s of AuNP/GQDs. (c) Ratio of different groups in GQDs and AuNP/GQDs. (d) 4f electron of Au. (e) Raman spectrum of AuNP/GQDs and GQDs. (f) Fourier transform infrared (FTIR) spectra of AuNP/GQDs and GQDs.

the surface plasmon resonance absorption of AuNPs. Excitation wavelength-dependent PL intensity experiments near the plasmon resonance peak of AuNP at 550 nm were performed to explore the optical properties of as-synthesized GQDs and AuNP/GQDs, as shown in Fig. 4(b). As the AuNP concentration increases, the excitation peak at 330 nm gradually moves to 368 nm [26,35]. The excitation peaks at 470 nm and 504 nm regularly disappear, forming a new excitation peak at 421 nm [Fig. 4(b)]. The PL spectra of GQDs, GQDs: AuNP = 400:1, 400:2, 400:3, and 400:4 excited by 300 nm, 325 nm, 368 nm, and 421 nm, respectively, are shown in Figs. 4(c)–4(f). Here GQDs and AuNPs respectively act as acceptors and donors for fluorescence resonance energy transfer. It is worth noting that the PL line shape of GQDs exhibits asymmetric and multiple PL peaks, which confirms the existence of numerous electron transition pathways of GQDs [36]. High concentration AuNPs lead to selective PL enhancement of graphene, a phenomenon also observed in graphene oxide [37]. As shown in Fig. 4(c), when the incident wavelength is 300 nm, the emission mode at 412 nm is significantly enhanced, and excitation peaks sprout at 436 nm. When the incident wavelength is 325 nm [Fig. 4(d)], PL enhanced emission peaks appear at 394 nm, 412 nm, 457 nm, and 485 nm. When the incident wavelength is 368 nm [Fig. 4(e)], PL enhancement peaks arise at 410 nm, 462 nm, and 493 nm. With the excitation wavelength increasing to 421 nm, selective PL enhancement is no longer evident, but an enhanced emission mode can still be found at 495 nm. In most cases, the plasmon effect does not bring about a new

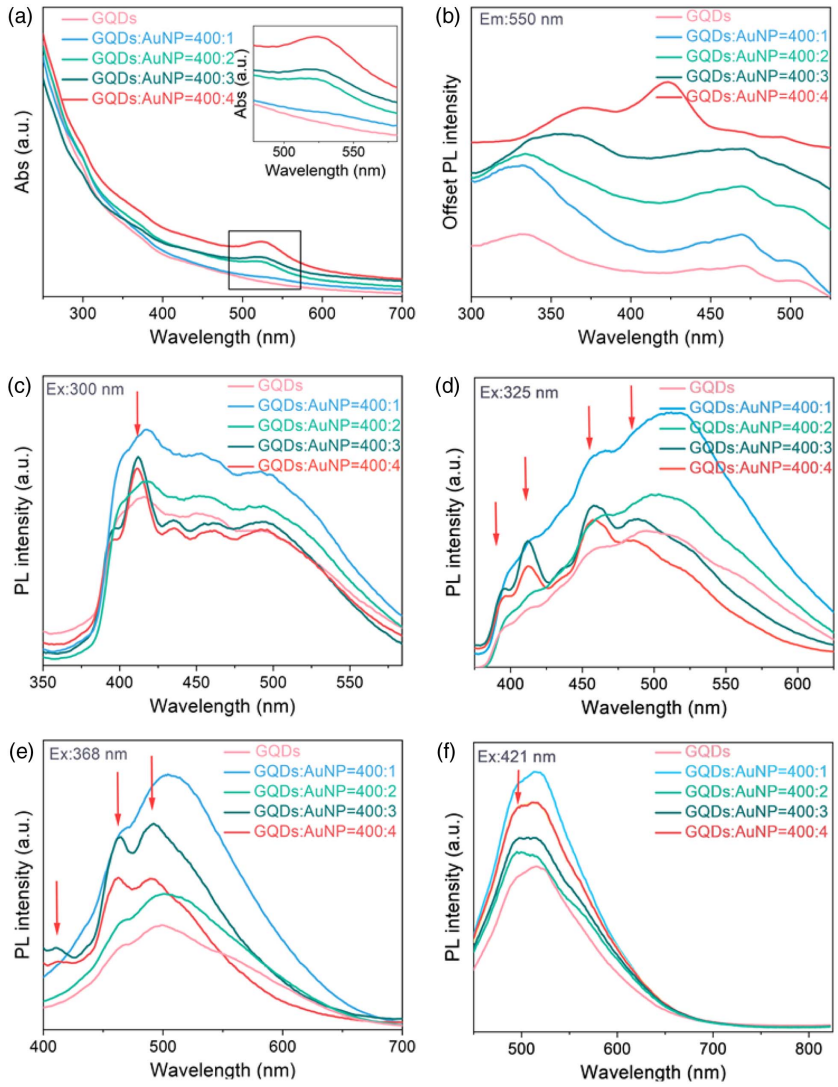

Fig. 4. (a) Ultraviolet-visible (UV-Vis) absorption spectra. (b) Excitation wavelength-dependent photoluminescence spectra with monitoring wavelength of 550 nm. Photoluminescence spectra of GQDs, GQDs:AuNP = 400:1, 400:2, 400:3, 400:4 excited by (c) 300 nm, (d) 325 nm, (e) 368 nm, and (f) 421 nm.

emission mode but rather enhances the selectivity of the original electron transition pathway of graphene. This enhancement effect is attributed to optical selection of different emissive sites on GQDs [38,39]. The optoelectronic properties of GQDs were determined by the π states of the sp^2 site. The π and π^* electronic levels of the sp^2 clusters lie within the bandgap of δ and δ^* states of the sp^3 matrix and are strongly localized [40,41]. The PL emission in GQDs resulted from the geminate recombination of localized electron–hole pairs in sp^2 clusters, which essentially behave as luminescence centers or chromophores. It has been proved that the short wavelength region is due to the electron–hole radiative recombination of intrinsic states, and the long wavelength region is due to the defect state emission from surface defects [26,38,42–46]. In a disordered carbon system, the PL peak intensity is linearly related to the sp^2 fraction [47]. The selective enhancement of the short wavelength region peak is attributed to the contribution of hot electrons from plasmons to electronic transition paths in GQDs. It is almost ineffective against emission from defect states. However, a low concentration addition of AuNP can lead to overall enhanced fluorescence, up to 2.67 times [Figs. 4(c)–4(f)], without selectively enhancing specific fluorescence emission modes due to the uniform and stable surface state of GQDs [26,48]. After the introduction of seldom AuNPs, fluorescence emission modes of GQDs did not change, which is in agreement with the first-principles calculation results that the adsorption of Au and GQDs is much weaker than that of Co, Ni, Pd, or Ti [49]. The electronic structure of GQDs would not be strongly perturbed by seldom AuNP but was essentially preserved in the weak binding physisorption regime.

TRPL measurements of AuNP/GQDs were performed to clearly investigate the impact of AuNP inclusion on GQDs. The corresponding normalized PL decay curves of GQDs and AuNP/GQDs are provided in Fig. 5(a). Based on previous

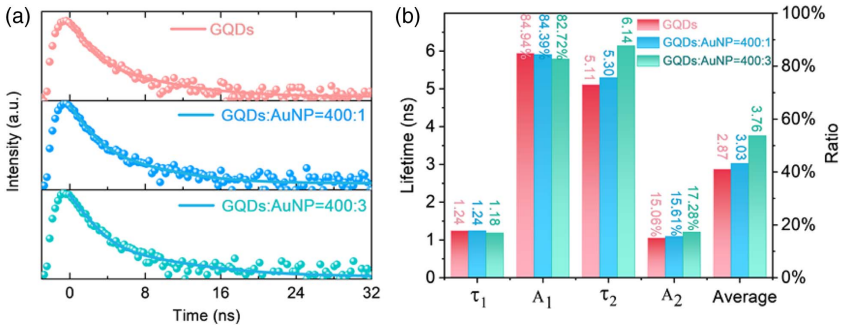

Fig. 5. (a) Photoluminescence lifetime of GQDs, GQDs:AuNP = 400:1 and 400:3. (b) Extracted photoluminescence lifetime parameters of GQDs and AuNP/GQDs.

studies, we fitted the decay curves by a multiexponential function with deconvolution of the instrument response function (IRF):

$$I(t) = \sum A_{\mathrm{i}} \exp\left(-\frac{t}{\tau_i}\right),$$

where $I(t)$ is the normalized PL intensity at delay time t, A_i $(i = 1, 2)$ is the weight factor (normalized by 100%) and represents the population contribution of each component, and τ_i $(i = 1, 2)$ is the decay time constant. The fitting results are presented in Fig. 5(b). The average lifetime increased from 2.87 ns to 3.76 ns with increasing concentration of AuNP. There is

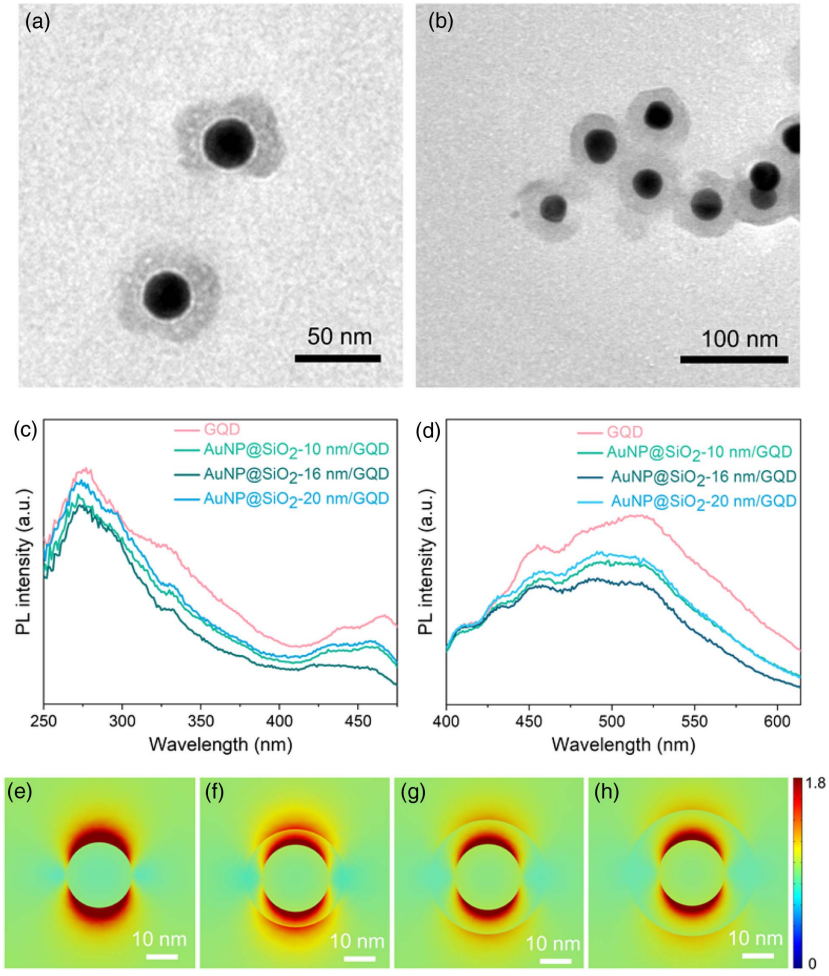

Fig. 6. (a), (b) TEM images of AuNPs coated with silicon oxide. (c) Excitation wavelength-dependent photoluminescence spectra and (d) photoluminescence spectra of GQDs and AuNP/GQDs coated with silicon oxide of different thicknesses, with excitation wavelength of 325 nm. Calculated electric field of (e) AuNP, (f) AuNP@SiO_2-10 nm, (g) AuNP@SiO_2-16 nm, and (h) AuNP@SiO_2-20 nm at electric dipole resonance (325 nm). The excitation light is along the z axis and polarized along the y axis in the calculations.

little effect on the shorter time constant (τ_1) with the addition of low concentration AuNP, while there is an evident increase of τ_1 by 20.16% with the addition of high concentration AuNP. We attribute this result to increased intrinsic exciton recombination [50]. The contribution of hot electrons to the extrinsic electronic state can lead to an increase in the values of PL intensity and shorter time constant (τ_1). With the addition of AuNP, generously implanted electrons fill higher energy state of GQD and relax directly to the ground state, leading to selective enhancement of the shorter wavelength. When AuNP is added at a low concentration, there is sufficient opportunity for electrons to relax to a lower energy level before returning to the ground state, leading to overall enhanced fluorescence.

When the metal NP is excited by light of a specific wavelength, the conduction electrons of the metal will oscillate collectively (i.e., plasma). The strong electromagnetic field associated with LSP resonance can be confined to the deep subwavelength space near the particle surface. Near-field enhancement of an electromagnetic field and hot electron injection are considered two potential reasons for PL enhancement. The surface of SiO_2 with a thickness of 10 nm has an electric field similar to that of an AuNP [Figs. 6(e) and 6(f)]. The electric field strength weakens as the thickness of silica increases [Figs. 6(f)–6(h)]. Silica can effectively isolate electron transfer but has little influence on electric field distribution [51,52]. As shown in Figs. 6(a) and 6(b), to distinguish which mechanism is responsible for the enhancement of PL silica layers with different thicknesses were wrapped on the AuNP to isolate a charge transfer path and adjust the near-field field strength. Figures 6(c) and 6(d) show that AuNP@SiO_2/GQDs demonstrate weaker PL emission, indicating that fluorescence enhancement is no longer possible after the charge transfer pathway is cut off. In our work, the PL enhancement of AuNP/GQDs is mainly due to the hot electron transfer.

To further illustrate the specific electron transfer reaction of AuNP, the band structure of the Au was calculated based on DFT [53,54], as shown in Fig. 7(a). The projected density of states (PDOS) [Fig. 7(b)] of AuNP was obtained from Fig. 7(a). There were two broad regions in PDOS, where a valence band appeared below −1.6 eV and a conduction band localized beyond 3 eV. The valence band is primarily composed of 5d electrons and small contribution from 6s and 5p states. In addition, the conduction band is mainly contributed by the electrons of s-p states. The band diagram of the AuNP/GQDs is schematically illustrated in Fig. 7(c). AuNP plays the role of a dipolar antenna, collecting incoming photons from its surroundings and concentrating the energy in the "hot spot." The work functions of pristine GQDs and AuNP are 4.5 eV and 5.2 eV, respectively [55,56]. The work functions of the highest occupied states and lowest unoccupied states of the graphite GQDs are estimated to be 6.14 eV and 2.7 eV, respectively [57]. Plasmon excitation energy (about 2.1 eV for AuNP) is above the Fermi level of GQDs, which enables the injection of hot electrons [58]. We generalize the AuNP-enhanced PL emission into three processes: (1) under visible light radiation, the electrons of metal are excited and have an energy higher than the Fermi level of GQDs [59]; (2) hot electrons from

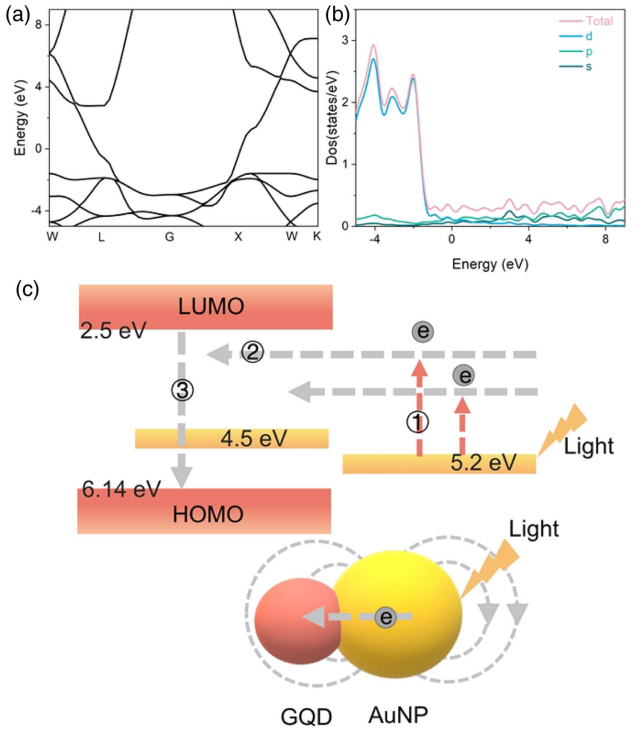

Fig. 7. (a) Calculated electronic band structure and (b) projected density of states (PDOS) of Au. (c) Band diagram of AuNP/GQDs.

AuNP are injected into the GQDs; (3) injected electrons in graphene relax to the ground state and radiate photons, leading to the enhanced fluorescence of AuNP/GQDs.

Pollution by heavy metal ions is a serious environmental problem. Heavy metal ion toxicity has been reported to cause many health issues to live beings and has motivated researchers to develop various strategies for the detection and removal of these heavy metal ions from aqueous systems to make water safe for use. In our work, AuNP/GQDs can be applied as a fluorescent probe for the assay of Cr^{3+}. To investigate the specificity of AuNP/GQDs as a fluorescent sensing platform for sensing Cr^{3+}, eight common metal ions such as Pb^{2+}, Cr^{3+}, Al^{3+}, Ni^{2+}, Co^{2+}, Fe^{2+}, Cu^{2+}, and Zn^{2+} were measured for the fluorescence responses under the same experimental conditions. As shown in Figs. 8(a) and 8(b), only Cr^{3+} can obviously quench the fluorescence of AuNP/GQDs, illustrating the high specificity of AuNP/GQDs for the Cr^{3+} sense. Figures 8(c) and 8(d) display the linear responses of the fluorescence intensity with the concentration of Cr^{3+} in the range of 1–400 μM (1 M = 1 mol/L), showing a correlation coefficient of 97.36%, which proves that this sensor had some potential to work reliably for the fluorescent probe. Actually, Cr^{3+} was adsorbed on the center of aromatic rings of GQDs, resulting in the reduction of π-conjugated regions and PL quenching, i.e., the strong adsorption with the charge transformation caused the fluorescence quenching [60,61]. When the detection concentration of Cr^{3+} was 50 ppb (parts per billion), the fluorescence intensity was reduced to 77.84%, much lower than the standard of the United States Environmental Protection

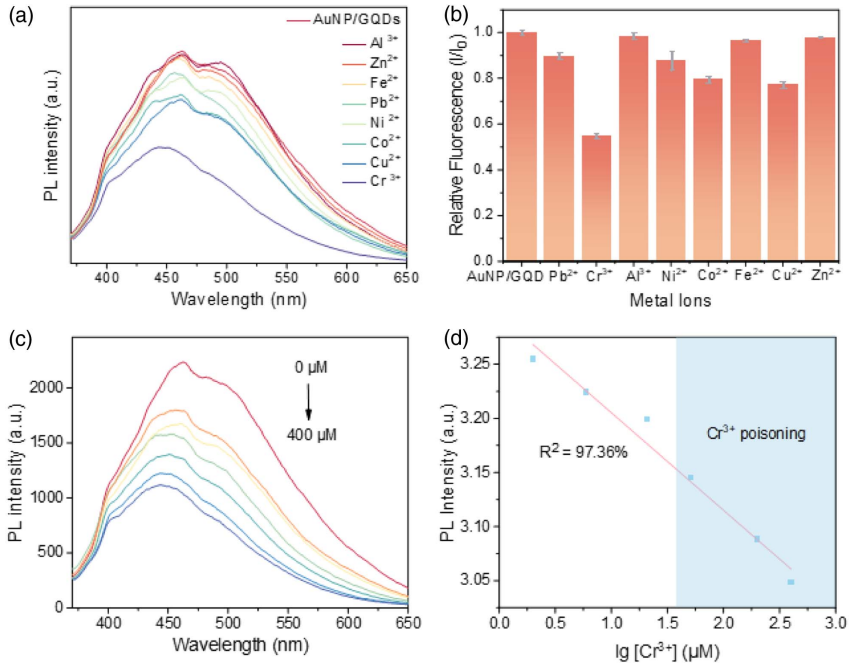

Fig. 8. (a) Fluorescence spectra of AuNP/GQDs for different heavy metal ions. (b) Different heavy metal ion detection effect statistics of AuNP/GQDs at a concentration of 50 μM. (c) Fluorescence spectra for detection of different concentrations of chromium ions. (d) Correlation coefficient of AuNP/GQDs and different concentrations of chromium ions; blue area corresponds to poison concentrations.

Agency (USEPA) for chromium in drinking water (100 ppb) [62]. AuNP/GQDs can easily judge whether a human exceeds the maximum allowable level of blood chromium content (13.4 μM). When AuNP/GQDs were used to detect Cr^{3+} concentration in human blood, there was a risk of Cr^{3+} poisoning when the fluorescence intensity was reduced to 56.06%.

3. EXPERIMENT

A. Reagents

Sodium hydroxide (98%) and L-ascorbic acid (AA, 99.99%) were purchased from Macklin. Hexadecyltrimethylammonium bromide (CTAB, 99.0%) and GQDs were purchased from Aladdin. Tetraethyl orthosilicate (TEOS, 28.4%), chloroauric acid (99.99%), sodium borohydride (96.0%), and hydrochloric acid (36%–38%) were purchased from Sinopharm Chemical Reagent Co., Ltd. (Shanghai, China).

B. Synthesis of AuNP/GQDs

AuNPs were prepared by a modified seed-mediated method. Typically, 0.5 mL of $HAuCl_4$ (5 mM) was added to 9.5 mL of CTAB (0.1 M). The mixture was stirred, followed by the quick addition of 0.6 mL of ice-cold $NaBH_4$ (10 mM). This seed solution was kept in an incubator chamber (30°C) for 2 h. 6 mL of the $HAuCl_4$ (5 mM) solution was added to 30 mL of CTAB (0.2 M). Then, 3.5 mL of AA (10 mM) and 1 mL of NaOH (1 M) were added to the mixture. Subsequently, 0.05 mL of the seed solution was rapidly injected. The solution was left at room temperature for 1 h to obtain Au nanospheres. Then Au nanospheres were centrifuged at 10,000 r/min for 15 min and dissolved in the same amount of water five times. Last, 40 μL AuNP was added to 200 μL GQDs, stirred for 12 h, and allowed to stand for more than 7 days to obtain AuNP/GQDs.

C. Synthesis of AuNP@SiO_2/GQDs

To synthesize the AuNP@SiO_2, 1 mL of CTAB, 20–50 μL TEOS, and 30 μL of NaOH were added to 4 mL AuNP. The solution was left at room temperature with mild stirring for 12 h, then centrifuged at 8500 r/min for 5 min, and dissolved in the same amount of water five times. Last, 40 μL AuNP@SiO_2 was added into 200 μL GQDs, stirred for 12 h, and allowed to stand for more than 7 days to obtain AuNP@SiO_2/GQDs.

D. Fluorescence Assay of Cr^{3+}

Specifically, 1 mL AuNP/GQDs solution was put into 8 mL of ultrapure water, followed by adding different amounts of Cr^{3+}. 1.25 μL of AuNP/GQDs was added to 5000 mL of heavy metal ions solution (50 μM) for heavy metal testing. The PL spectrum of Figs. 8(b) and 8(c) was measured 8 h after mixing.

E. Sample Characterization

TEM, HRTEM, and HADDF-STEM images and the SAED pattern were obtained using an FEI Tecnai G2 F20 X-Twin microscope operated at an accelerating voltage of 200 kV. The UV-Vis absorption spectra were measured by a Thermo Scientific Evolution 220 UV-Vis instrument, while the PL spectra were measured by a Hitachi F-460, and PL decay curves were assessed by an Edinburgh FLS1000 spectrophotometer under an excitation wavelength of 365 nm. In addition, the XPS spectra were measured using a Thermo Scientific K-Alpha+. The SERS spectra were acquired with a 514 nm wavelength laser source using a Horiba LabRAM HR Evolution. We put the sample into the capillary tube, collected three ranges in

different areas, and took the average. FTIR spectroscopy absorption spectra were measured by a Thermo Scientific Evolution NICOLET iS50.

F. Computational Details

In this work, all DFT calculations were performed using generalized gradient approximation (GGA) and the Perdew–Burke–Ernzerh (PBE) exchange-correlation function. The employed periodic cell dimension was $a = b = c = 4.17$ Å. The corresponding Brillouin zone sampling k-point set-mesh parameters were $4 \times 4 \times 4$.

4. CONCLUSION

In conclusion, the plasmon resonance caused by the AuNP as an antenna can considerably boost light absorption larger than GQDs and thus enhance the PL emission of GQDs. The control experiment of isolating the adiabatic electron transfer path and adjusting the near-field strength proves that the energy transfer caused by plasmon resonance in AuNP/GQDs is the main reason for the PL enhancement of AuNP to GQDs. Furthermore, we can selectively enhance the fluorescence of GQDs by controlling the addition of AuNP. AuNP/GQDs show great potential in the detection of Cr^{3+}, with a correlation coefficient of 97.36%. The concept in this work is an important step forward in using plasmonic particles to selectively enhance the PL of GQDs and clarify the mechanism. We expect that it would bring more possibilities to take advantage of plasmonic resonance enhanced fluorescence for highly sensitive probes.

Funding. State Key Laboratory of Pulsed Power Laser Technology (KY21C604); College of Electronic Engineering (KY22C213, KY21C220); National Natural Science Foundation of China (61871389); Research Plan Project of the National University of Defense Technology (ZK18-01-02).

Disclosures. The authors declare no conflicts of interest.

Data Availability. Data underlying the results presented in this paper are not publicly available at this time but may be obtained from the authors upon reasonable request.

REFERENCES

1. K. Zhao, L. Ge, T. I. Wong, X. Zhou, and G. Lisak, "Gold-silver nanoparticles modified electrochemical sensor array for simultaneous determination of chromium(III) and chromium(VI) in wastewater samples," Chemosphere **281**, 130880 (2021).
2. Y. Wang, Y. Ma, Q. Zhao, L. Hou, and Z. Han, "Polyoxometalate-based crystalline catalytic materials for efficient electrochemical detection of Cr(VI)," Sens. Actuators B **305**, 127469 (2020).
3. S. Zhao, X. Lai, F. Liu, and L. Chen, "Carbon dots combined with masking agent for high selectivity detection of Cr(VI) to overcome interference associated challenges," Ecotoxicol. Environ. Safety **244**, 114069 (2022).
4. T. P. Rao, S. Karthikeyan, B. Vijayalekshmy, and C. S. P. Iyer, "Speciative determination of chromium(VI) and chromium(III) using flow-injection on-line preconcentration and flame atomic-absorption spectrometric detection," Anal. Chim. Acta **369**, 69–77 (1998).
5. S. A. Miscoria, C. Jacq, T. Maeder, and R. M. Negri, "Screen-printed electrodes for electroanalytical sensing, of chromium VI in strong acid media," Sens. Actuators B **195**, 294–302 (2014).
6. S. K. Tammina and Y. L. Yang, "Highly sensitive and selective detection of 4-nitrophenol, and on-off-on fluorescence sensor for Cr (VI) and ascorbic acid detection by glucosamine derived n-doped carbon dots," J. Photochem. Photobiol. A **387**, 112134 (2020).
7. H. J. Lim, H. Jin, B. Chua, and A. Son, "Clustered detection of eleven phthalic acid esters by fluorescence of graphene quantum dots displaced from gold nanoparticles," ACS Appl. Mater. Interfaces **14**, 4186–4196 (2022).
8. L. Xu, W.-Q. Huang, W. Hu, K. Yang, B.-X. Zhou, A. Pan, and G.-F. Huang, "Two-dimensional MoS_2-graphene-based multilayer van der Waals heterostructures: enhanced charge transfer and optical absorption, and electric-field tunable Dirac point and band gap," Chem. Mater. **29**, 5504–5512 (2017).
9. S. Kim, S. W. Hwang, M.-K. Kim, D. Y. Shin, D. H. Shin, C. O. Kim, S. B. Yang, J. H. Park, E. Hwang, S.-H. Choi, G. Ko, S. Sim, C. Sone, H. J. Choi, S. Bae, and B. H. Hong, "Anomalous behaviors of visible luminescence from graphene quantum dots: interplay between size and shape," ACS Nano **6**, 8203–8208 (2012).
10. H. Kang, D. Y. Kim, and J. Cho, "Top-down fabrication of luminescent graphene quantum dots using self-assembled Au nanoparticles," ACS Omega **8**, 5885–5892 (2023).
11. X. Duan, C. Wang, A. Pan, R. Yu, and X. Duan, "Two-dimensional transition metal dichalcogenides as atomically thin semiconductors: opportunities and challenges," Chem. Soc. Rev. **44**, 8859–8876 (2015).
12. C. Yu, Z. He, X. Song, Q. Liu, L. Gao, B. Yao, T. Han, X. Gao, Y. Lv, Z. Feng, and S. Cai, "High-frequency flexible graphene field-effect transistors with short gate length of 50 nm and record extrinsic cut-off frequency," Phys. Status Solidi R **12**, 1700435 (2018).
13. C. Joyce, S. M. Fothergill, and F. Xie, "Recent advances in gold-based metal enhanced fluorescence platforms for diagnosis and imaging in the near-infrared," Mater. Today Adv. **7**, 100073 (2020).
14. A. Perveen, L. Deng, A. Muravitskaya, D. Yang, A. Movsesyan, S. Gaponenko, S. Chang, and H. Zhong, "Enhanced emission of *in-situ* fabricated perovskite-polymer composite films on gold nanoparticle substrates," Opt. Mater. Express **10**, 1659–1674 (2020).
15. A. Minopoli, B. Della Ventura, B. Lenyk, F. Gentile, J. A. Tanner, A. Offenhaeusser, D. Mayer, and R. Velotta, "Ultrasensitive antibody-aptamer plasmonic biosensor for malaria biomarker detection in whole blood," Nat. Commun. **11**, 6134 (2020).
16. H. Cheng, Y. Lu, D. Zhu, L. Rosa, F. Han, M. Ma, W. Su, P. S. Francis, and Y. Zheng, "Plasmonic nanopapers: flexible, stable and sensitive multiplex PUF tags for unclonable anti-counterfeiting applications," Nanoscale **12**, 9471–9480 (2020).
17. M. Tavakkoli Yaraki, M. Wu, E. Middha, W. Wu, S. Daqiqeh Rezaei, B. Liu, and Y. N. Tan, "Gold nanostars-AIE theranostic nanodots with enhanced fluorescence and photosensitization towards effective image-guided photodynamic therapy," Nano-Micro Lett. **13**, 58 (2021).
18. A. Perveen, A. Movsesyan, S. M. Abubakar, F. Saeed, S. Hussain, A. Raza, Y. Xu, A. Subramanian, Q. Khan, and W. Lei, "*In-situ* fabricated and plasmonic enhanced $MACsPbBr_3$-polymer composite perovskite film based UV photodetector," J. Mol. Struct. **1279**, 134962 (2023).
19. Y. X. Zhang, A. Dragan, and C. D. Geddes, "Broad wavelength range metal-enhanced fluorescence using nickel nanodeposits," J. Phys. Chem. C **113**, 15811–15816 (2009).
20. T. Ozel, P. L. Hernandez-Martinez, E. Mutlugun, O. Akin, S. Nizamoglu, I. O. Ozel, Q. Zhang, Q. H. Xiong, and H. V. Demir, "Observation of selective plasmon-exciton coupling in nonradiative energy transfer: donor-selective versus acceptor-selective plexcitons," Nano Lett. **13**, 3065–3072 (2013).
21. L. Ma, Y.-L. Chen, X.-P. Song, D.-J. Yang, H.-X. Li, S.-J. Ding, L. Xiong, P.-L. Qin, and X.-B. Chen, "Structure-adjustable gold nanoingots with strong plasmon coupling and magnetic resonance for improved photocatalytic activity and SERS," ACS Appl. Mater. Interfaces **12**, 38554–38562 (2020).
22. L. Ma, Y.-L. Chen, D.-J. Yang, S.-J. Ding, L. Xiong, P.-L. Qin, and X.-B. Chen, "Gap-dependent plasmon coupling in Au/AgAu hybrids for improved SERS performance," J. Phys. Chem. C **124**, 25473–25479 (2020).

23. L. Ma, Y.-L. Chen, D.-J. Yang, H.-X. Li, S.-J. Ding, L. Xiong, P.-L. Qin, and X.-B. Chen, "Multi-interfacial plasmon coupling in multigap (Au/AgAu)@CdS core-shell hybrids for efficient photocatalytic hydrogen generation," Nanoscale **12**, 4383–4392 (2020).
24. L. Ma, Y.-L. Chen, X. Yang, H.-X. Li, S.-J. Ding, H.-Y. Hou, L. Xiong, P.-L. Qin, and X.-B. Chen, "Growth behavior of Au/Cu_{2-x} S hybrids and their plasmon-enhanced dual-functional catalytic activity," CrystEngComm **21**, 5610–5617 (2019).
25. Y. Shen, T. He, W. Wang, Y. Zhan, X. Hu, B. Yuan, and X. Zhou, "Fluorescence enhancement on silver nanoplates at the single- and sub-nanoparticle level," Nanoscale **7**, 20132–20141 (2015).
26. G. Eda, Y. Y. Lin, C. Mattevi, H. Yamaguchi, H. A. Chen, I. S. Chen, C. W. Chen, and M. Chhowalla, "Blue photoluminescence from chemically derived graphene oxide," Adv. Mater. **22**, 505–509 (2010).
27. Y. Q. Sun, S. Q. Wang, C. Li, P. H. Luo, L. Tao, Y. Wei, and G. Q. Shi, "Large scale preparation of graphene quantum dots from graphite with tunable fluorescence properties," Phys. Chem. Chem. Phys. **15**, 9907–9913 (2013).
28. M. K. Thakur, C.-Y. Fang, Y.-T. Yang, T. A. Effendi, P. K. Roy, R.-S. Chen, K. K. Ostrikov, W.-H. Chiang, and S. Chattopadhyay, "Microplasma-enabled graphene quantum dot-wrapped gold nanoparticles with synergistic enhancement for broad band photodetection," ACS Appl. Mater. Interfaces **12**, 28550–28560 (2020).
29. G. Haider, P. Roy, C. W. Chiang, W. C. Tan, Y. R. Liou, H. T. Chang, C. T. Liang, W. H. Shih, and Y. F. Chen, "Electrical-polarization-induced ultrahigh responsivity photodetectors based on graphene and graphene quantum dots," Adv. Funct. Mater. **26**, 620–628 (2016).
30. P. Wang, Z. G. Liu, X. Chen, F. L. Meng, J. H. Liu, and X. J. Huang, "UV irradiation synthesis of an Au-graphene nanocomposite with enhanced electrochemical sensing properties," J. Mater. Chem. A **1**, 9189–9195 (2013).
31. C. T. Chien, S. S. Li, W. J. Lai, Y. C. Yeh, H. A. Chen, I. S. Chen, L. C. Chen, K. H. Chen, T. Nemoto, S. Isoda, M. W. Chen, T. Fujita, G. Eda, H. Yamaguchi, M. Chhowalla, and C. W. Chen, "Tunable photoluminescence from graphene oxide," Angew. Chem. Int. Ed. **51**, 6662–6666 (2012).
32. B. Park, S. J. Kim, J. S. Sohn, M. S. Nam, S. Kang, and S. C. Jun, "Surface plasmon enhancement of photoluminescence in photochemically synthesized graphene quantum dot and Au nanosphere," Nano Res. **9**, 1866–1875 (2016).
33. H. Zhang, S. Chen, X. Quan, H. Yu, and H. Zhao, "*In situ* controllable growth of noble metal nanodot on graphene sheet," J. Mater. Chem. **21**, 12986–12990 (2011).
34. R. R. Gaddam, S. Mukherjee, N. Punugupati, D. Vasudevan, C. R. Patra, R. Narayan, and R. V. S. N. Kothapalli, "Facile synthesis of carbon dot and residual carbon nanobeads: Implications for ion sensing, medicinal and biological applications," Mater. Sci. Eng. C **73**, 643–652 (2017).
35. P. Byeongho, K. Sun Jun, S. Ji Soo, N. Min Sik, K. Shinill, and J. Seong Chan, "Surface plasmon enhancement of photoluminescence in photo-chemically synthesized graphene quantum dot and Au nanosphere," Nano Res. **9**, 1866–1875 (2016).
36. P. Anger, P. Bharadwaj, and L. Novotny, "Enhancement and quenching of single-molecule fluorescence," Phys. Rev. Lett. **96**, 113002 (2006).
37. N. T. Lan, D. T. Chi, N. X. Dinh, N. D. Hung, H. Lan, P. A. Tuan, L. H. Thang, N. N. Trung, N. Q. Hoa, T. Q. Huy, N. V. Quy, T. T. Duong, V. N. Phan, and A. T. Le, "Photochemical decoration of silver nanoparticles on graphene oxide nanosheets and their optical characterization," J. Alloys Compd. **615**, 843–848 (2014).
38. S. Zhu, J. Zhang, S. Tang, C. Qiao, L. Wang, H. Wang, X. Liu, B. Li, Y. Li, W. Yu, X. Wang, H. Sun, and B. Yang, "Surface chemistry routes to modulate the photoluminescence of graphene quantum dots: from fluorescence mechanism to up-conversion bioimaging applications," Adv. Funct. Mater. **22**, 4732–4740 (2012).
39. Q. Liu, B. Guo, Z. Rao, B. Zhang, and J. R. Gong, "Strong two-photon-induced fluorescence from photostable, biocompatible nitrogen-doped graphene quantum dots for cellular and deep-tissue imaging," Nano Lett. **13**, 2436–2441 (2013).
40. C. Mathioudakis, G. Kopidakis, P. C. Kelires, P. Patsalas, M. Gioti, and S. Logothetidis, "Electronic and optical properties of a-C from tight-binding molecular dynamics simulations," Thin Solid Films **482**, 151–155 (2005).
41. C. W. Chen and J. Robertson, "Nature of disorder and localization in amorphous carbon," J. Non-Cryst. Solids **227**, 602–606 (1998).
42. L. Bao, Z. L. Zhang, Z. Q. Tian, L. Zhang, C. Liu, Y. Lin, B. P. Qi, and D. W. Pang, "Electrochemical tuning of luminescent carbon nanodots: from preparation to luminescence mechanism," Adv. Mater. **23**, 5801–5806 (2011).
43. K. P. Loh, Q. L. Bao, G. Eda, and M. Chhowalla, "Graphene oxide as a chemically tunable platform for optical applications," Nat. Chem. **2**, 1015–1024 (2010).
44. S. J. Zhu, J. H. Zhang, C. Y. Qiao, S. J. Tang, Y. F. Li, W. J. Yuan, B. Li, L. Tian, F. Liu, R. Hu, H. N. Gao, H. T. Wei, H. Zhang, H. C. Sun, and B. Yang, "Strongly green-photoluminescent graphene quantum dots for bioimaging applications," Chem. Commun. **47**, 6858–6860 (2011).
45. D. Y. Pan, J. C. Zhang, Z. Li, and M. H. Wu, "Hydrothermal route for cutting graphene sheets into blue-luminescent graphene quantum dots," Adv. Mater. **22**, 734–738 (2010).
46. S. Zhu, J. Zhang, C. Qiao, S. Tang, Y. Li, W. Yuan, B. Li, L. Tian, F. Liu, R. Hu, H. Gao, H. Wei, H. Zhang, H. Sun, and B. Yang, "Strongly green-photoluminescent graphene quantum dots for bioimaging applications," Chem. Commun. **47**, 6858–6860 (2011).
47. J. Robertson, "Recombination and photoluminescence mechanism in hydrogenated amorphous carbon," Phys. Rev. B **53**, 16302–16305 (1996).
48. L. L. Li, G. H. Wu, G. H. Yang, J. Peng, J. W. Zhao, and J. J. Zhu, "Focusing on luminescent graphene quantum dots: current status and future perspectives," Nanoscale **5**, 4015–4039 (2013).
49. P. A. Khomyakov, G. Giovannetti, P. C. Rusu, G. Brocks, J. van den Brink, and P. J. Kelly, "First-principles study of the interaction and charge transfer between graphene and metals," Phys. Rev. B **79**, 195425 (2009).
50. S.-H. Song, M. Jang, H. Yoon, Y.-H. Cho, S. Jeon, and B.-H. Kim, "Size and pH dependent photoluminescence of graphene quantum dots with low oxygen content," RSC Adv. **6**, 97990–97994 (2016).
51. Z. Gao, L. Li, Y. Ge, and Q. Chen, "Enhanced AC magnetic properties of Fe-based soft magnetic composites coated with an electrically insulated SiO_2-ZrO_2 layer," J. Mater. Sci. **32**, 14944–14955 (2021).
52. P. Frach, H. Bartzsch, D. Gloess, M. Fahland, and F. Haendel, "Electrically insulating Al_2O_3 and SiO_2 films for sensor and photovoltaic applications deposited by reactive pulse magnetron sputtering, hollow cathode arc activated deposition and magnetron-PECVD," Surf. Coat. Technol. **202**, 5680–5683 (2008).
53. H. A. Alluhaybi, S. K. Ghoshal, B. O. Alsobhi, and W. N. W. Shamsuri, "Electronic and optical correlation effects in bulk gold: role of spin-orbit coupling," Comput. Condens. Matter **18**, e00360 (2019).
54. A. Dal Corso and A. M. Conte, "Spin-orbit coupling with ultrasoft pseudopotentials: application to Au and Pt," Phys. Rev. B **71**, 115106 (2005).
55. S. H. Cheng, T. M. Weng, M. L. Lu, W. C. Tan, J. Y. Chen, and Y. F. Chen, "All carbon-based photodetectors: an eminent integration of graphite quantum dots and two dimensional graphene," Sci. Rep. **3**, 2694 (2013).
56. R. R. Ford, "Work functions of gold and silver films—surface potentials of mercury and xenon," Trans. Faraday Soc. **67**, 216–221 (1971).
57. G. Konstantatos and E. H. Sargent, "PbS colloidal quantum dot photoconductive photodetectors: transport, traps, and gain," Appl. Phys. Lett. **91**, 2800805 (2007).
58. B. L. Liu, L. Chen, G. Liu, A. N. Abbas, M. Fathi, and C. W. Zhou, "High-performance chemical sensing using Schottky-contacted chemical vapor deposition grown mono layer MoS_2 transistors," ACS Nano **8**, 5304–5314 (2014).
59. C. Clavero, "Plasmon-induced hot-electron generation at nanoparticle/metal-oxide interfaces for photovoltaic and photocatalytic devices," Nat. Photonics **8**, 95–103 (2014).

60. J. Li, Z. Wang, J. Yang, X. Xia, R. Yi, J. Jiang, W. Liu, J. Chen, L. Chen, and J. Xu, ""On-off-on" fluorescence switch of graphene quantum dots: a cationic control strategy," Appl. Surf. Sci. **546**, 149110 (2021).
61. J. Yang, P. Li, Z. Song, J. Li, H. Yang, F. Yan, L. Li, C. Xu, J. Chen, and L. Chen, "Graphene quantum dots via ion modification for improving photoluminescence stability in aqueous solution with heavy metal ions," Appl. Surf. Sci. **593**, 153367 (2022).
62. T. Y. Gu, M. Dai, D. J. Young, Z. G. Ren, and J. P. Lang, "Luminescent Zn(II) coordination polymers for highly selective sensing of Cr(III) and Cr(VI) in water," Inorg. Chem. **56**, 4668–4678 (2017).